Chapter 1

MZO in variable velocity media

To check the accuracy of the MZO in variable velocity media presented in chapters 1 and 2, in this chapter I introduce a new, independent method to obtain the impulse response of the MZO operator. This separate method is based on the decomposition of the migration-to-zero-offset operator into prestack migration followed by zero-offset modeling (Deregowski and Rocca, 1981; Deregowski, 1985), and uses a fast algorithm to compute the traveltime maps necessary for modeling wave propagation in a general 2-D medium (Van Trier and Symes, 1990). The next section compares the kinematics of the impulse responses generated with each method and shows that in depth variable velocity the two operators are extremely similar.

1.1 A second method for computing MZO kinematics in variable velocity media

An alternate algorithm for computing the impulse response of MZO using finite-difference traveltime maps is based on the principle that MZO is the combination of two processes: full prestack migration and zero-offset modeling. In a constant velocity medium, this definition allows for an analytical formulation of the MZO kinematic operator that is identical with the DMO after NMO formulation (Popovici and Biondi, 1989). The algorithm used to investigate the MZO operator in variable velocity media follows the definition of the MZO method and can be divided in two parts (Deregowski and Rocca, 1981; Popovici 1990):

- *Constructing the full prestack migration depth model.* The depth model represents the position in space of all points that can generate a given impulse in a constant-offset section. For a constant velocity medium this step is equivalent to constructing the migration ellipse. For a variable velocity medium, the loci of points with equal traveltime from source to receiver form a curve resembling an ellipse or a superposition of several ellipses.

- *Zero-offset modeling.* Given the depth model, we raytrace back at 90 degrees from the reflector, to model the zero-offset data. The intersection of the ray with the surface gives the x-coordinate of the MZO operator, while the traveltime along the raypath provides the zero-offset time-coordinate.

Considering the MZO process as the combination of full prestack migration followed by zero-offset modeling, the MZO impulse response can be computed using finite-difference traveltime maps (Popovici, 1991). The traveltime algorithm (Van Trier and Symes, 1990), is based on solving the acoustic wave equation in the high-frequency approximation (with the eikonal equation). The velocity model used for MZO has only a depth variation, though the traveltime algorithm can handle lateral velocity variation as well. The velocity is assumed to be a continuous function of depth. For media where velocity is not a linear function of depth, the MZO impulse response may have serious variations from the constant velocity case, and triplications can occur in the normally ellipse-shaped MZO impulse response (Popovici, 1990).

1.1.1 Two adjoint MZO operators

Spreading data along the MZO impulse response is identical to summing along a adjoint curve. For zero-offset migration in a constant velocity medium, this statement is equivalent to saying that spreading the data over circles produces a result identical to summing along hyperbolas. From a computational point of view, the spreading operator (an ellipse for DMO, a circle for constant velocity migration) is called a *PUT* operator, meaning that the operator takes a time sample and puts it in all the adjacent traces. The adjoint summation operator (a hyperbola for constant velocity migration) is called a *GET* operator because it gets the input from the adjacent traces.

By using finite-difference traveltime maps, the GET and PUT operators can be calculated in similar ways, beginning with the same six steps:

1. Given a velocity model $v(x, z)$, compute a traveltime map for the source.

2. Compute a traveltime map with the source in the receiver location, given the same velocity model.

3. Sum the two traveltime maps. Thus, in each location of the grid we have the sum of the traveltime from source to receiver $T_{co}(x, z)$.

4. The gradient of the constant-offset traveltime field $T_{co}(x, z)$ is a vector that has the same direction as the zero-offset ray. In other words, the vector perpendicular to a constant-offset isochrone bisects the angle between the ray coming from the source and the one returning to the receiver. Find the ray direction for the zero-offset case for each grid point, by calculating the gradient of the constant-offset traveltime map in each point of the grid.

5. Using the gradient table, compute for each grid location the surface coordinate of the zero-offset $X_0(x,z)$, which is equivalent to finding the intersection of the surface with the zero-offset ray.

6. Using the gradient table, compute for each grid location the zero-offset traveltime $T_0(x,z)$ along each zero-offset ray.

Thus far, the algorithm is identical for the two adjoint operators. At this point, the three tables generated using the same velocity model are;

$$\begin{cases} T_{co}(x,z), & \text{the constant-offset traveltime field.} \\ X_0(x,z), & \text{the zero-offset surface coordinate field.} \\ T_0(x,z), & \text{the zero-offset time field.} \end{cases}$$

The PUT operator is obtained by associating each value of $T_{co}(x,z)$ with a pair of coordinates $(T_0(x,z), X_0(x,z))$. In other words, for a given value of the constant-offset traveltime, we find an isochrone $t_h = T_{co}(x_h, z_h)$ of coordinates (x_h, z_h) and the values of the $X_0(x_h, z_h)$ and $T_0(x_h, z_h)$ associated with that curve. The GET operator can be defined similarly, by associating each value of $T_0(x,z)$ with a pair of coordinates $(T_{co}(x,z), X_0(x,z))$. In other words, for a given value of the zero-offset time field, we find an isochrone $t_0 = T_0(x_0, z_0)$ of coordinates (x_0, z_0) and the values of the $X_0(x_0, z_0)$ and $T_{co}(x_0, z_0)$ associated with that curve.

1.2 MZO impulse response in variable velocity media

I applied the MZO operator to a series of depth-variable velocity models. Figure 1.2 shows in the left panel the constant-offset traveltimes map corresponding to the velocity model in the right panel. The velocity has a jump from 2000 m/s to 4000 m/s. Figure 1.3 shows the corresponding impulse response of the MZO phase-shift operator. The kinematics of the MZO operator obtained using traveltime maps is plotted on top of the seismic section, as isolated dots. The two main branches of the operator coincide, but the traveltime MZO operator also contains triplications due to overturned rays. The phase-shift MZO in my implementation does not handle diving rays. Figure 1.1 explains schematically the kinematic origin of the main branches of the MZO operator.

Figure 1.1 shows the kinematics of the traveltimes in a constant-offset section and a step function interval velocity profile. The velocity model is similar to the one described by Hawkins (1994) for the Central Graben area in the North Sea. The thick line in Figure 1.1 represents the right half of an isochrone in the constant-offset traveltime map, corresponding to an impulse at 1.1 seconds and a half offset of 500 m. The isochrone describes the location of all the possible reflection surfaces in the depth model that could generate an impulse response at 1.1 seconds for the given half

offset of 500 meters. In other words is represents the result of applying full prestack depth migration to an impulse situated at 1.1 seconds. It is also the first step needed to build the MZO operator.

There are three sections along the isochrone, that can be separated from a kinematic point of view. The branch in Figure 1.1, corresponding to the area A, is associated with traveltimes going only through the top velocity layer. The branch corresponding to the area B is associated with traveltimes traversing both velocity layers. The branch corresponding to the area C are head waves, propagating through the first velocity layer and the gray area which represents a transition layer between the two velocity horizons.

The second step in building the MZO operator is zero-offset modeling. This step is accomplished by raytracing back from the isochrone, the rays being perpendicular to the isochrone. The dashed lines in Figure 1.1, represent the zero-offset rays. The traveltimes along the rays give the time correction for the MZO operator, while their intersection with the surface give the spatial correction. The zero-offset rays corresponding to branch A in Figure 1.1 contribute to the branch A of the MZO operator in Figure 1.3. In the same way, the branch B in Figure 1.1, is mapped on the MZO operator in the area B. The triplications of the MZO operator in the area C are due to the head waves that are contoured by the branch C on the isochrone in Figure 1.1.

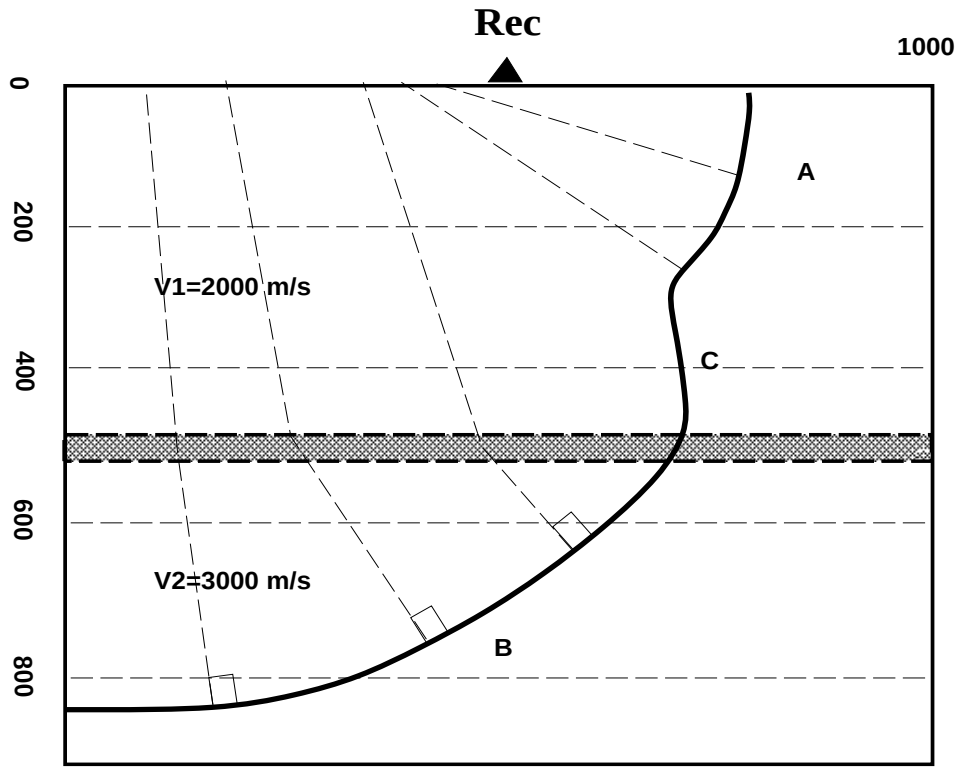

Figure 1.1: The isochrone that generates the MZO impulse response in the first velocity model. The isochrone corresponds to the prestack migration kinematics of an impulse at 1.1 seconds and a half offset of 580 m. The dashed lines represent the zero-offset rays. chapter3-DepthSurface [NR]

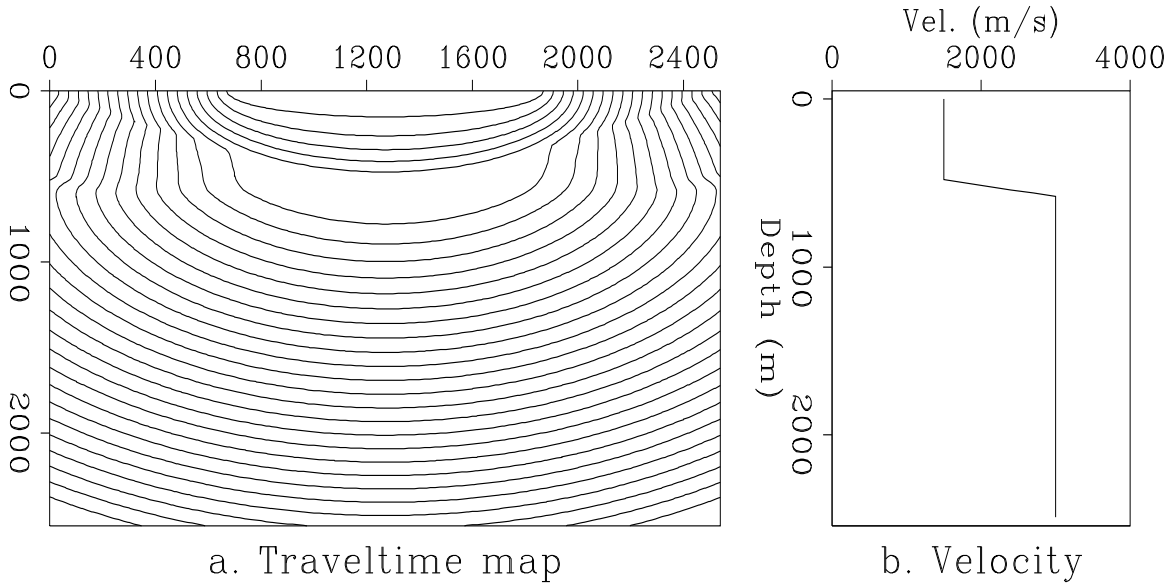

Figure 1.2: Constant-offset traveltime map and the corresponding velocity model. chapter3-C3f1 [ER]

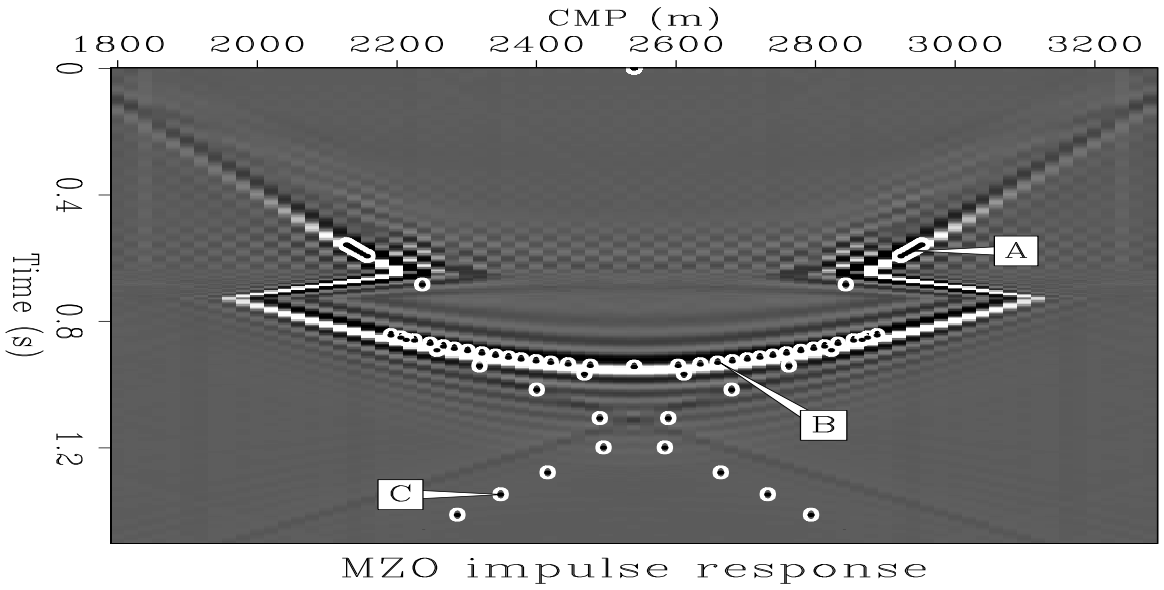

Figure 1.3: The MZO kinematics using traveltime maps superimposed on phase-shift MZO kinematics. The branch A corresponds to rays traveling in the upper velocity layer, while the branch B corresponds to rays traveling through both velocity layers. The triplications in branch C are due to the transition zone. chapter3-C3f2phase [CR]

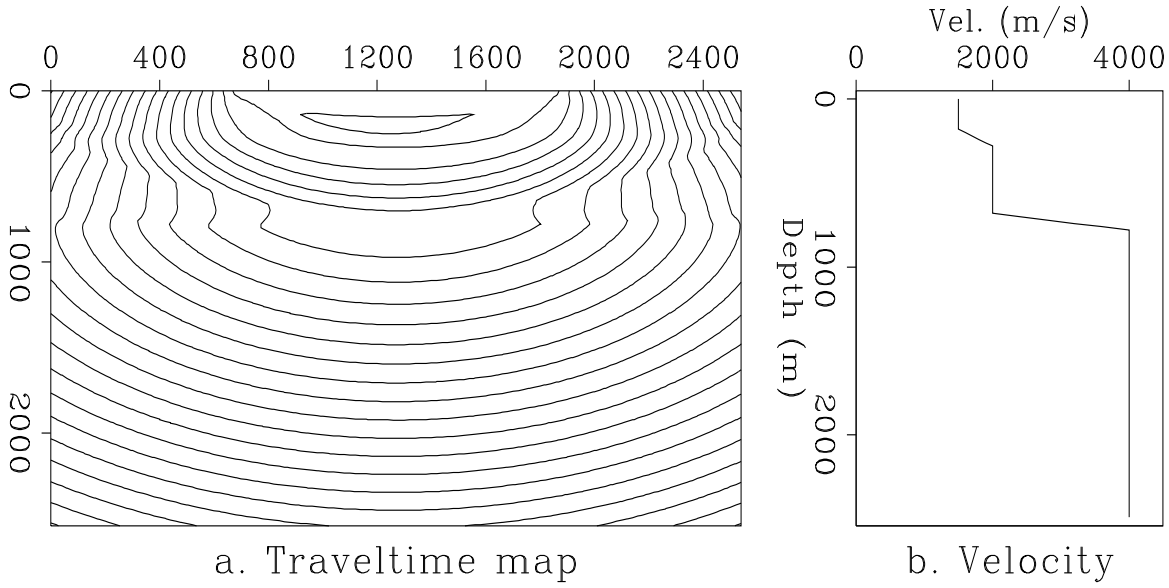

Figure 1.4: Constant-offset traveltime map and the corresponding velocity model. chapter3-C3f3 [ER]

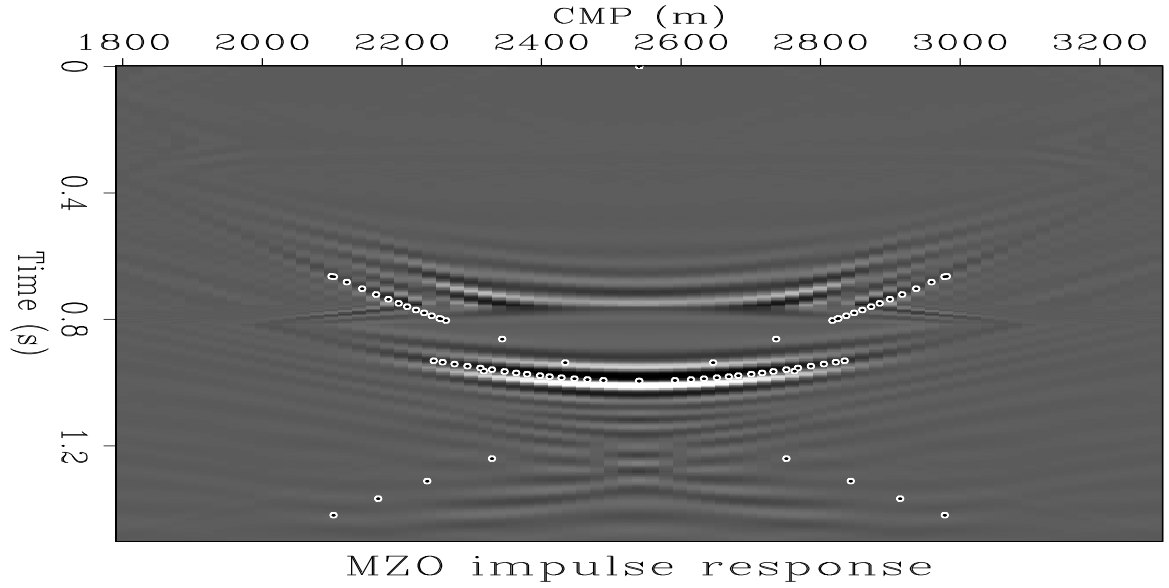

Figure 1.5: Comparison of MZO impulse responses.
The MZO kinematics of the impulse response obtained using traveltime maps is superimposed on the impulse response of the integral MZO. chapter3-C3f4 [CR]

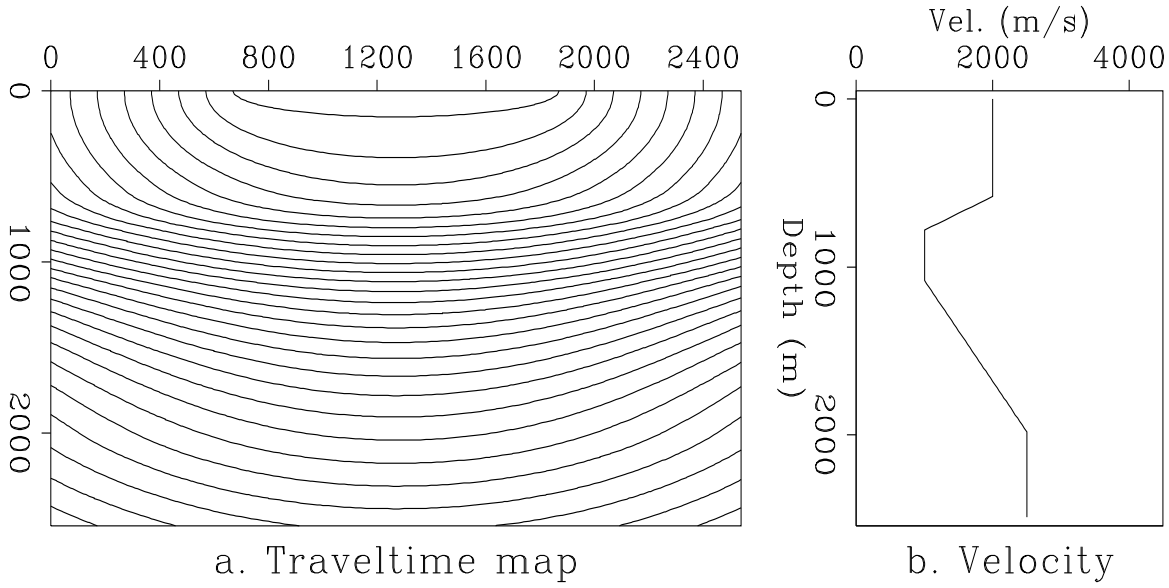

Figure 1.6: Constant-offset traveltime map and the corresponding velocity model. chapter3-C3f5 [ER]

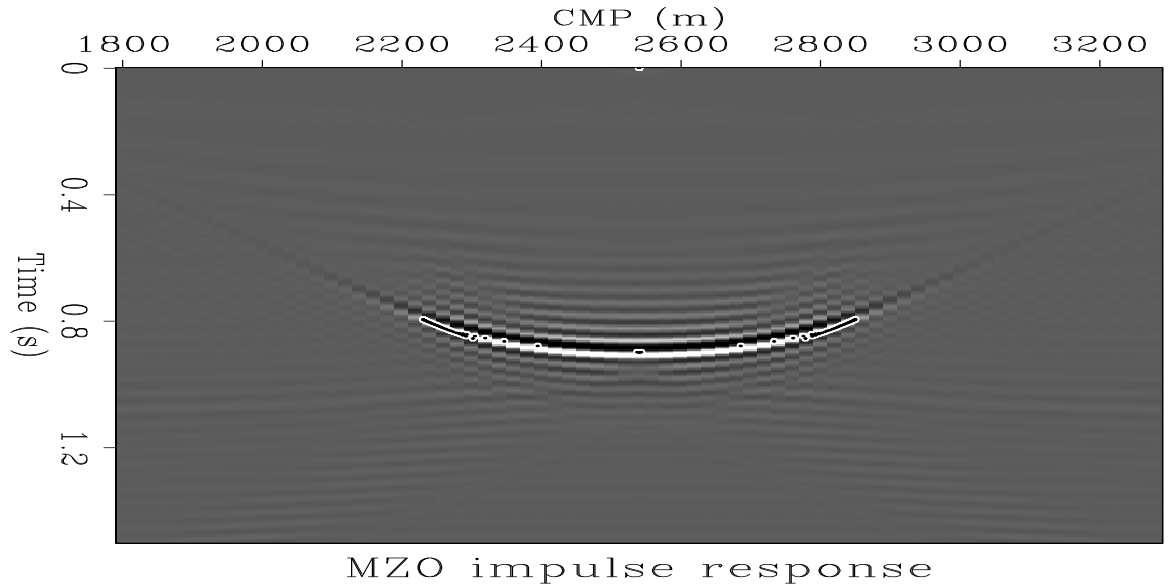

Figure 1.7: Comparison of MZO impulse responses.
The MZO kinematics of the impulse response obtained using traveltime maps is superimposed on the impulse response of the integral MZO. chapter3-C3f6 [CR]

1.2.1 MZO applied to synthetic data

I applied the MZO phase-shift operator to a simple synthetic model containing three dipping reflectors in a depth-variable velocity medium. The dip of the reflectors is 30, 45 and 60 degrees. Figure 1.8 shows in the left panel the zero-offset section,

in the middle panel the farther common-offset section and in the right panel the interval velocity model. The velocity model has two distinct velocity layers, 1500 m/s and 3000 m/s, separated at a depth of 1000 m. The maximum offset used was 3250 meters ($h_{max} = 1625$). Figure 1.9 shows the stacked data, the left panel after NMO and DMO, the right panel after MZO. Surprisingly, NMO and DMO do a good job at stacking the dipping reflectors in the second velocity layer. The events stack even better after MZO, especially at higher dips, though MZO in depth variable velocity is a second order correction. The phase-shift MZO algorithm also filters some steep dipping events, because the frequency domain implementation has an existence condition that limits the dip range with velocity.

Figures 1.10 and 1.11 show several CMP gathers through the original, NMO corrected, NMO and DMO corrected, and finally MZO corrected data. As expected, NMO overcorrects the data, and DMO undercorrects the diffractions, but surprisingly it has the opposite effect on the dipping reflectors. The events sloping upward are dipping reflectors while the events sloping downward are diffraction hyperbola branches. For this particular velocity model, a simple squeezing modification to the DMO algorithm that does not take into account the multiple branching of the operator could degrade the stacked image. In Figure 1.11 the MZO corrected data shows that there is a better event alignment for the farther offsets, but for the close offsets NMO followed by DMO offer a very good stacking solution.

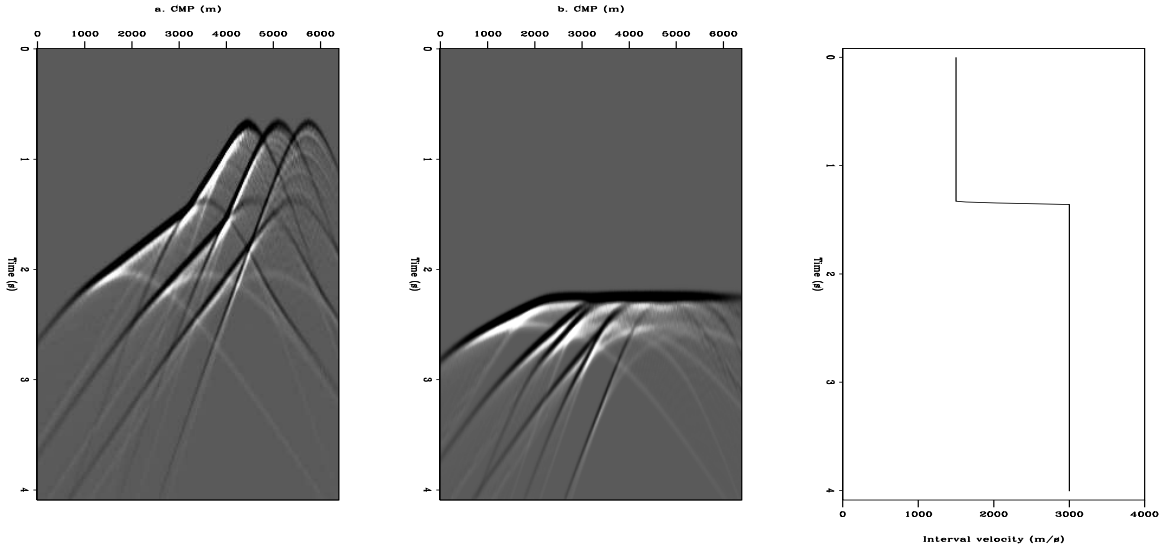

Figure 1.8: Three dipping reflectors in a zero-offset section, last offset section and the interval velocity model.
a. Zero-offset section.
b. Highest offset common-offset section.
c. Interval velocity model. chapter3-diff3ZOLAMig [ER]

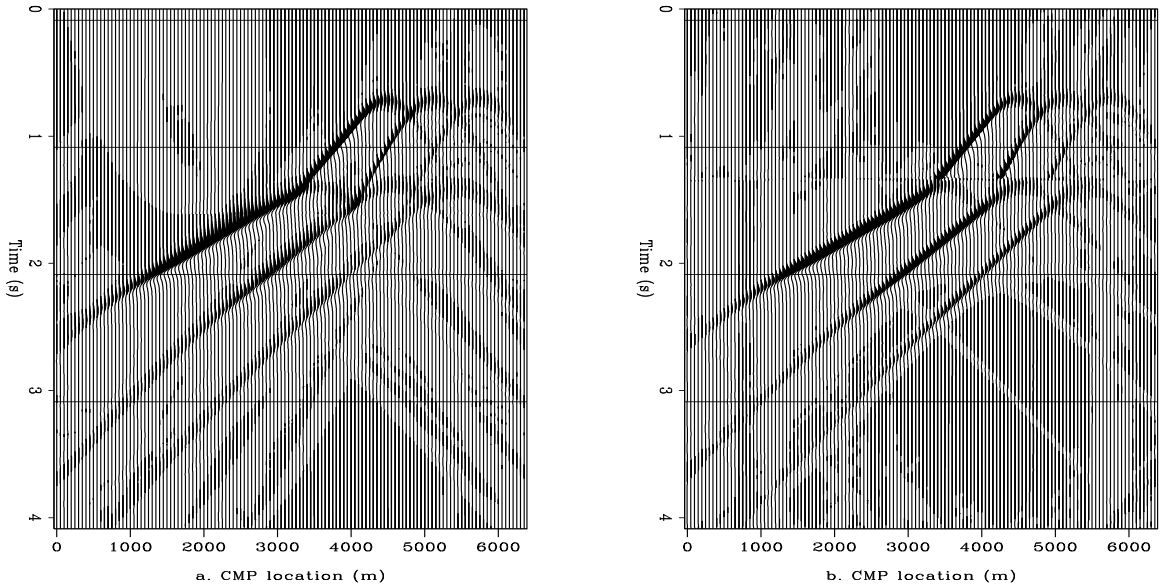

Figure 1.9: Stacked sections after DMO and MZO.
a. NMO and DMO corrected data, stacked.
b. MZO and stack. chapter3-diffsynDMst [ER]

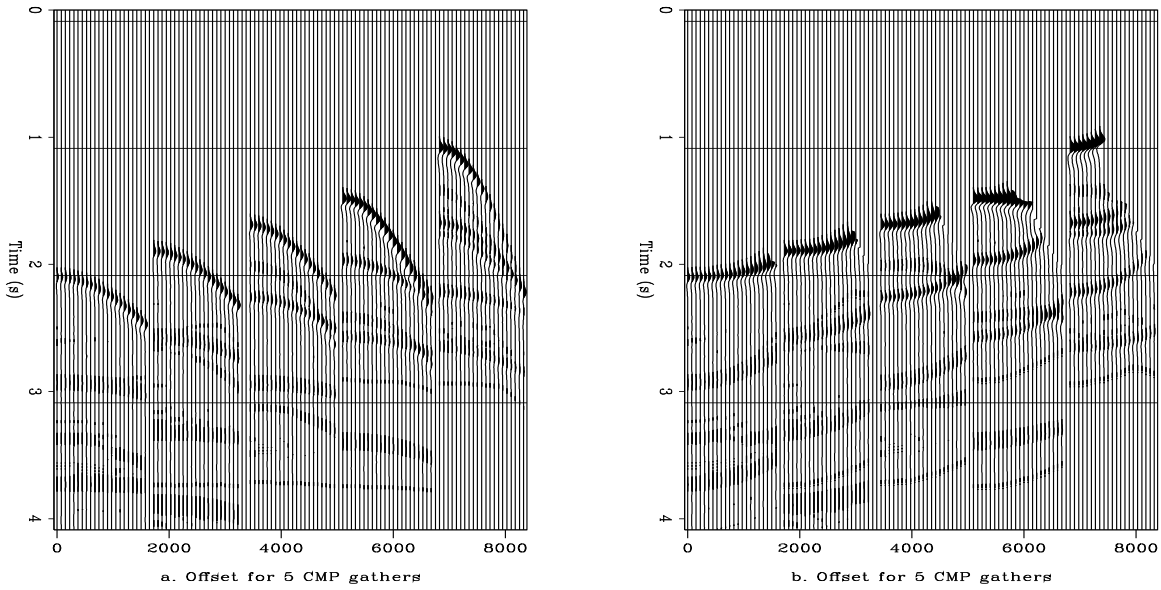

Figure 1.10: Comparison between original input data and NMO corrected data.
a. Several input CMP gathers.
b. CMP gathers after NMO. chapter3-diffsynINcmp5 [ER]

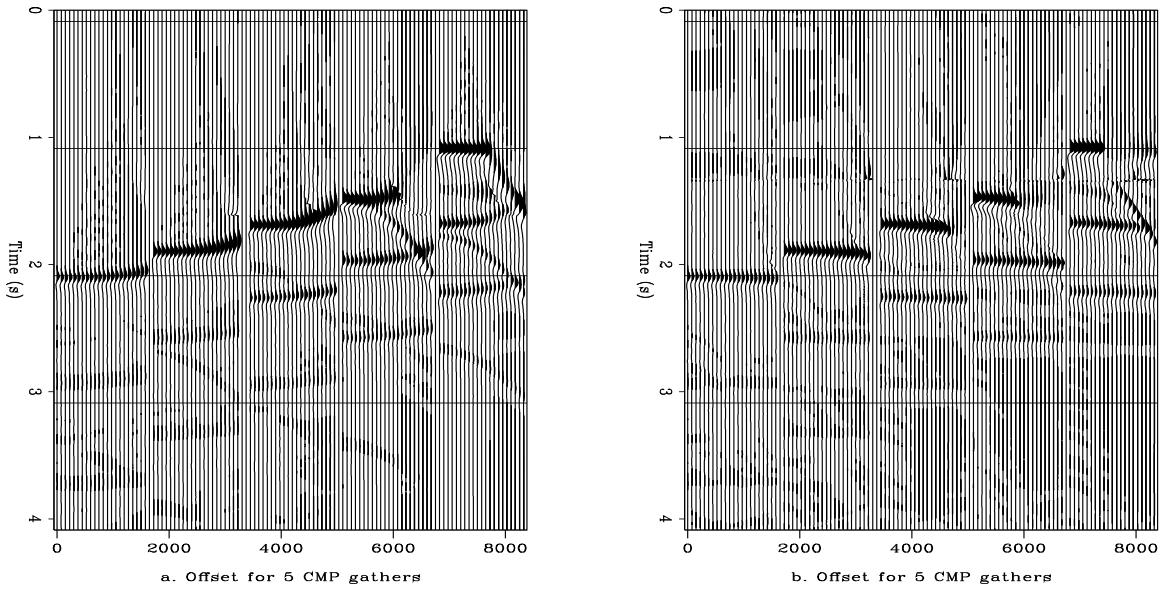

Figure 1.11: Comparison between DMO and MZO.
a. Several CMP gathers after NMO and DMO.
b. CMP gathers after MZO. chapter3-diffsynDMcmp5 [CR]

1.3 Handling the lateral velocity variations

The DSR prestack migration equation, though defined for depth variable velocity, can be used to image media with strong velocity variations using a phase-shift plus

interpolation (PSPI) or split-step correction. The split-step method is based on applying a phase-shift correction to the extrapolated wavefield, correction that attempts to compensate for the lateral velocity variations. Since the equations for DSR and MZO are extremely similar, I show first how to extend DSR prestack migration to lateral velocity media and exemplify the method by applying the new algorithm to the Marmousi dataset. The same method is then used to extend MZO to media lateral velocity variations. The results are not satisfactory and therefore a second approach is proposed for MZO in $v(x,z)$ showing much better results. The second approach is based on using NMO to correct for lateral velocity variations, inverse NMO with a laterally invariant velocity, and MZO using the same laterally invariant velocity to convert the common-offset sections to zero-offset. This approach shows better imaging for the Marmousi dataset than the standard sequence of NMO followed by DMO.

1.3.1 Split-step prestack migration

From Chapter 1, I rewrite the two basic definitions for zero-offset and prestack phase-shift migration, as a starting point for further demonstrations. The prestack migration equation (**??**) was formulated as

$$p(t=0,k_y,h=0,z) = \int d\omega \int dk_h \; e^{ik_{zp}(\omega,k_y,k_h)z} p(\omega,k_y,k_h,z=0),$$

where $p(\omega,k_y,k_h,z=0)$ is the 3-D Fourier transform of the field $p(t,y,h,z=0)$ recorded at the surface.

The zero-offset migration (**??**) was formulated as

$$p(t=0,k_y,z) = \int d\omega_0 \; e^{ik_z(\omega_0,k_y)z} p(\omega_0,k_y,z=0)$$

where $p(\omega_0,k_y,z=0)$ is the 2-D Fourier transform of the field $p(t,y,z=0)$. The phase $k_{zp}(\omega,k_y,k_h)$ in the prestack migration case, and $k_z(\omega_0,k_y)$ in the zero-offset migration case, are defined as

$$\begin{aligned} k_{zp}(\omega,k_y,k_h) &= -\text{sign}(\omega)\left[\sqrt{\frac{\omega^2}{v^2}-\frac{1}{4}(k_y+k_h)^2}+\sqrt{\frac{\omega^2}{v^2}-\frac{1}{4}(k_y-k_h)^2}\right] \\ k_z(\omega_0,k_y) &= -2\,\text{sign}(\omega_0)\sqrt{\frac{\omega_0^2}{v^2}-\frac{k_y^2}{4}}. \end{aligned}$$

For zero-offset migration, the idea of a split-step correction appeared first in Gazdag and Sguazzero's (1984) PSPI algorithm, but it did not become a standalone technique until Stoffa et al. (1990) reversed the order of the algorithm, permitting the correction to be applied only once. The schematic flow of the two algorithms is shown in Figure 1.12, and the split-step correction is represented by the box containing the $e^{-\frac{\omega}{v(x,z)}\Delta z}$ term.

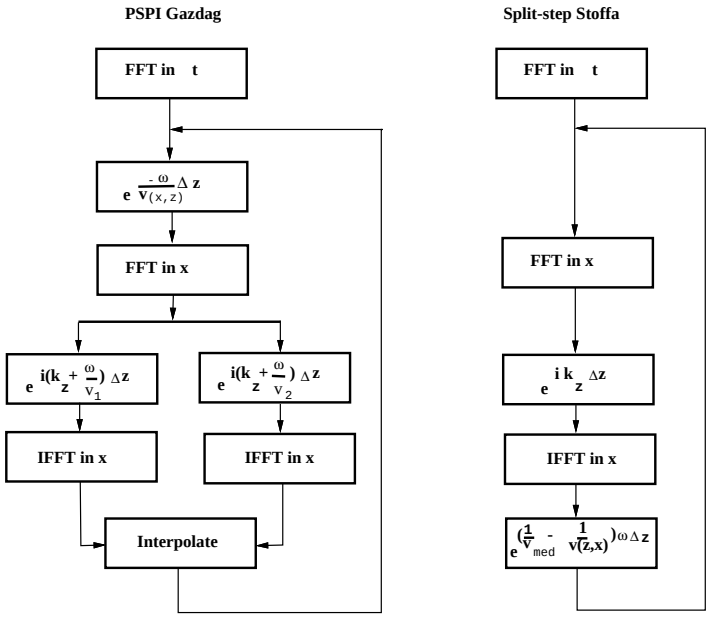

Figure 1.12: The two Fourier migration algorithms.
a) Phase Shift Plus Interpolation (PSPI).
b) Split-step Fourier Migration. chapter3-gazsplit [NR]

Gazdag and Sguazzero (1984) implement a technique in the PSPI algorithm to ensure that all the zero dips (corresponding to the case $k_x = 0$) are downward continued without distortion. The technique consists of multiplying the wavefield $P(x, z, \omega)$ with the phase-shift correction factor

$$e^{-i\frac{\omega}{v(x,z)}\Delta z}$$

prior to the Fourier transformation along the X axis. The downward extrapolation phase incorporates another correction factor

$$e^{i\frac{\omega}{v_1}\Delta z}$$

where the subscript v_1 denotes one of the constant velocities used in the downward extrapolation step. When the velocity varies only in depth $v(z)$, the two terms cancel each other. When the reflectors are flat ($k_x = 0$), the extrapolation term becomes

$$e^{-i\sqrt{\frac{\omega^2}{v^2}-k_x^2}\Delta z} = e^{-i\frac{\omega}{v}\Delta z}$$

and is cancelled by the multiplication with the phase-shift correction factor

$$e^{i\frac{\omega}{v_1}\Delta z}.$$

As a result, the zero-dip reflections are downward continued with the correct laterally varying phase-shift

$$e^{-i\frac{\omega}{v(x,z)}\Delta z}.$$

The same result can be obtained via the Stoffa et al. (1990) algorithm, where the phase-correction term is contained in a single term, as follows:

$$e^{i(\frac{1}{v_m}-\frac{1}{v(x,z)})\omega\Delta z}.$$

The difference is that the downward extrapolation is done with a single velocity and the perturbation slowness phase shift is performed after the downward extrapolation step.

For prestack migration, the two square roots in the phase term represent specifically the extrapolation term for the source and for the receiver. In other words if we downward extrapolate first the source, and second the receiver, we need in each case a different phase-correction term. The phase-correction term includes a laterally varying velocity function, $v_g(x,z)$ for the geophone-field continuation and $v_s(x,z)$ for the source-field continuation. A minor problem arises in the fact that the DSR prestack migration equation (**??**) is defined in midpoint and offset coordinates, while the velocity is defined in shot and geophone coordinates. We can easily go from one system to another using the transformation relations (**??**) defined in Chapter 1. The split-step correction term becomes

$$e^{i(\frac{2}{v_m}-\frac{1}{v_g(x_s,z)}-\frac{1}{v_g(x_g,z)})\omega\Delta z}$$

where x_s and x_g are the shot and geophone surface coordinates. In midpoint-offset coordinates the split-step correction term becomes

$$e^{i(\frac{2}{v_m}-\frac{1}{v(y-h,z)}-\frac{1}{v(y+h,z)})\omega\Delta z}.$$

In other words, for each midpoint y, use the velocity located at $y-h$ (the source location) and the velocity located at $y+h$ (the receiver location). A diagram of the prestack migration split-step algorithm is represented in Figure 1.13. The last box represents the multiplication with the split-step correction exponential term, where the slowness difference Δs is defined as

$$\Delta s(y,h,z) = \frac{2}{v_m} - \frac{1}{v(y-h,z)} - \frac{1}{v(y+h,z)}.$$

The DSR split-step migration algorithm was applied to the Marmousi data, a well known prestack synthetic dataset generated by the Institut Français du Pétrole. The Marmousi dataset is based on a real geologic model from the Cuanza basin in Angola (Bourgeois et al, 1991). The geological model of the basin consists of a deltaic sediment interval deposited upon a saliferous evaporitic series. The sediments are affected by normal growth faults caused by the salt creep. Under the salt there is a folded carbonate sedimentation series forming a structural hydrocarbon trap. The challenge presented to the exploration geophysicists it to image the hydrocarbon trap. The complex velocity model, with strong lateral velocity variations, is shown in Figure 1.14a. Figure 1.14b shows the near-offset section with a half-offset $h = 100m$.

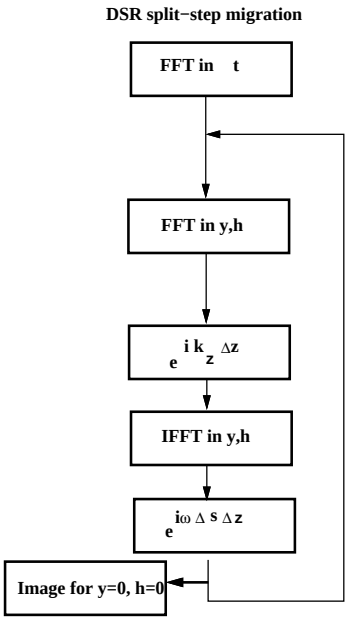

Figure 1.13: DSR split-step prestack migration algorithm. chapter3-DSRsplit [NR]

Figure 1.15a shows the result of zero-offset split-step migration applied to the near-offset section. The near full offset is 200 meters (h=100 m). Applying a zero-offset algorithm to a non-zero offset section obviously introduces errors in the imaging results, and the target area is poorly imaged. In comparison, the DSR split-step prestack migration algorithm produces an excellent image of the hydrocarbon trap, shown in Figure 1.15b. These encouraging results suggested that a split-step correction applied to the depth variable MZO algorithm could provide a viable extension to $v(x, z)$.

1.3.2 Extending MZO to laterally varying velocity media

Continuing the parallel between the DSR equation (??) and the MZO equation (??), the split-step correction can be applied to the migration to zero-offset algorithm in the same way as it was applied to the DSR prestack migration equation. The split-step phase-correction term includes a laterally varying velocity function, $v_g(x,t)$ for the geophone-field continuation and $v_s(x,t)$ for the source-field continuation. To correct for the fact that the MZO equation (??) is defined in midpoint and offset coordinates while the velocity is defined in shot and geophone coordinates, we can easily go from one system to another using the transformation relations (??) defined in Chapter 1. The split-step correction term becomes

$$e^{i(\frac{2}{v_m}-\frac{1}{v_g(x_s,t)}-\frac{1}{v_g(x_g,t)})\omega\Delta t}$$

where x_s and x_g are the shot and geophone surface coordinates. In midpoint-offset coordinates the split-step correction term becomes

$$e^{i(\frac{2}{v_m}-\frac{1}{v(y-h,t)}-\frac{1}{v(y+h,t)})\omega\Delta t}.$$

In other words, for each midpoint y, use the velocity located at $y-h$ (the source location) and the velocity located at $y+h$ (the receiver location). Unfortunately, the results obtained applying the split-step correction to MZO show that while there are some promising aspects to this approach, the split step correction presented here has to be improved further.

The upper part of the stacked section is better defined in the MZO-split-step algorithm than the NMO and stack section shown in Figure 1.17b or the NMO, DMO and stacked section shown in Figure 1.18a. The lower part though, is stacked to the wrong location , and therefore after zero-offset split-step migration the basement is imaged in the wrong location. I conclude that the split-step phase-shift correction I used for MZO is lacking an extra term, that would account for the correct event positioning.

Another approach to tackle the lateral velocity variation is to use the standard NMO to handle the first order lateral velocity variation, and MZO to handle the second order depth variable dip correction. The processing sequence is comprised of three steps:

- NMO with a laterally varying $V_{rms}(x,t)$.
- Inverse NMO with an average depth varying velocity $V_{arms}(t)$.
- MZO using the interval velocity from the preceding step.

As can be seen in Figures 1.18 and 1.19 this second method produces better results than the standard NMO followed by DMO processing sequence. The top boundary of the anticlinal structure around 2000 m is better defined, the bottom of the salt at about 2500 m has better continuity, the target structure is better imaged, and in general the image is better focused after MZO.

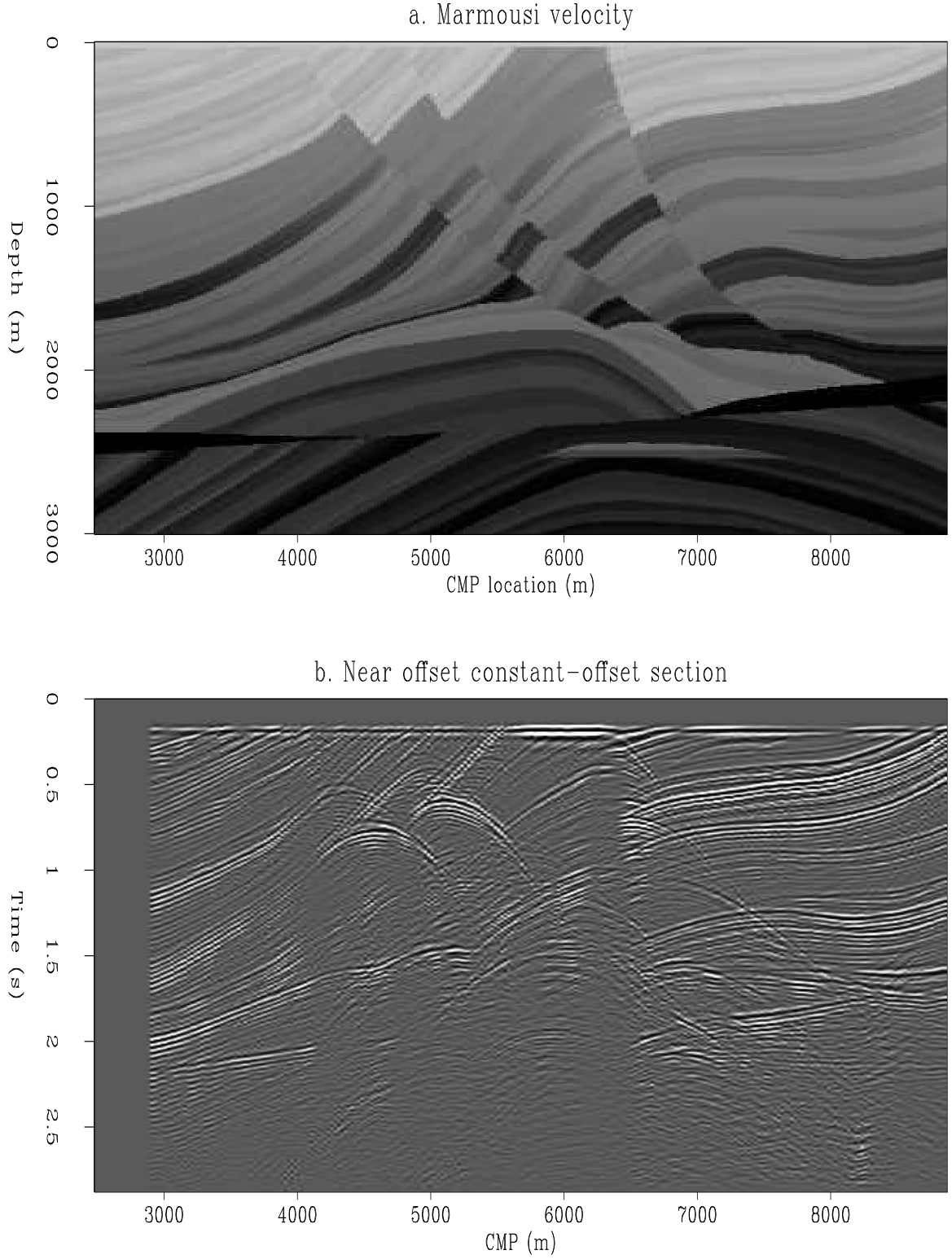

Figure 1.14: Marmousi velocity model and near-offset section.
a. Marmousi velocity model.
b. Near-offset section (h=100 m). chapter3-marmVelandNO [ER]

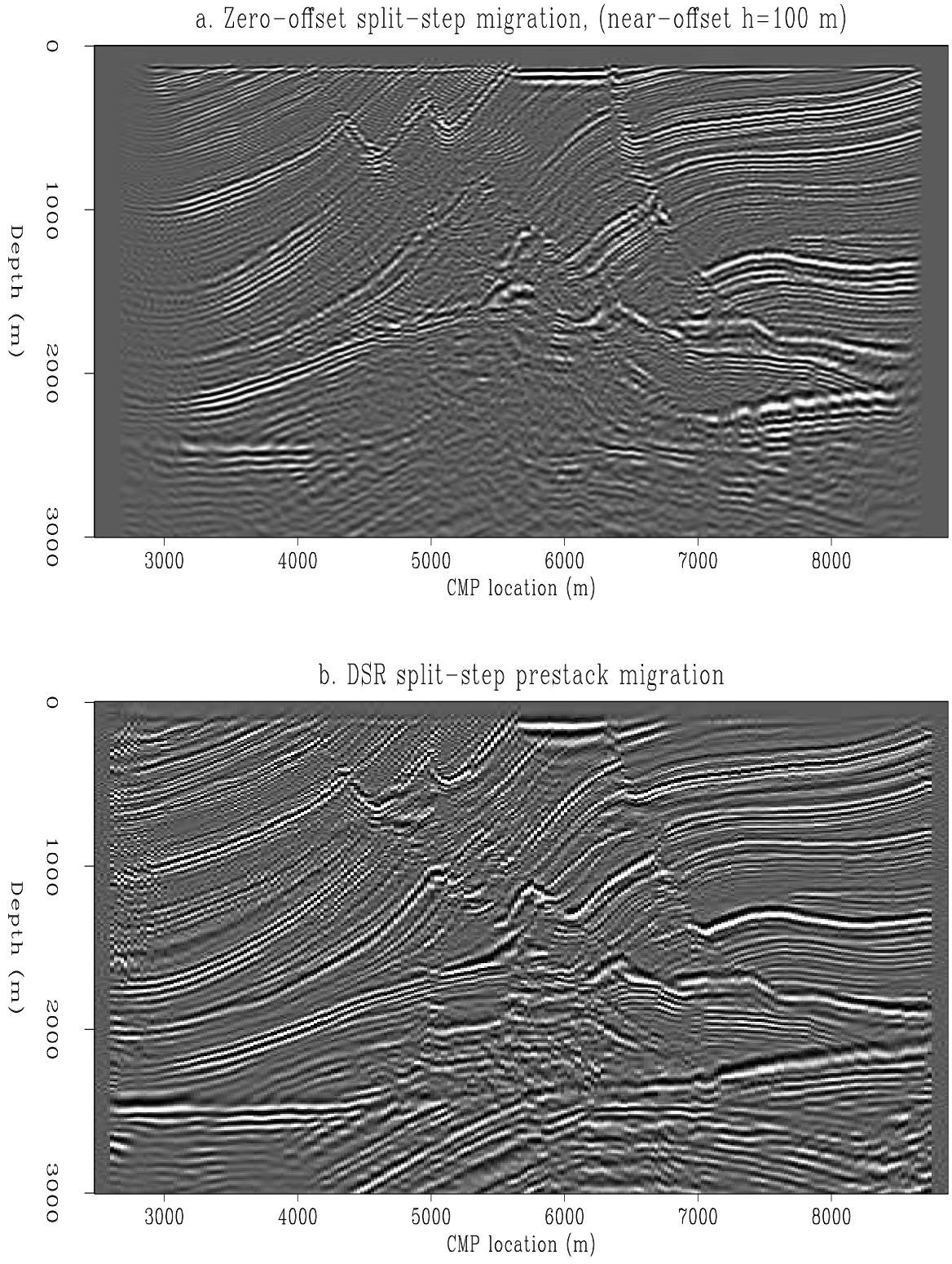

Figure 1.15: Zero-offset and prestack migration of the Marmousi.
a. Zero-offset migration of the near-offset section.
b. Prestack migration using DSR with a split-step term. chapter3-ZOandDSRsplit [CR]

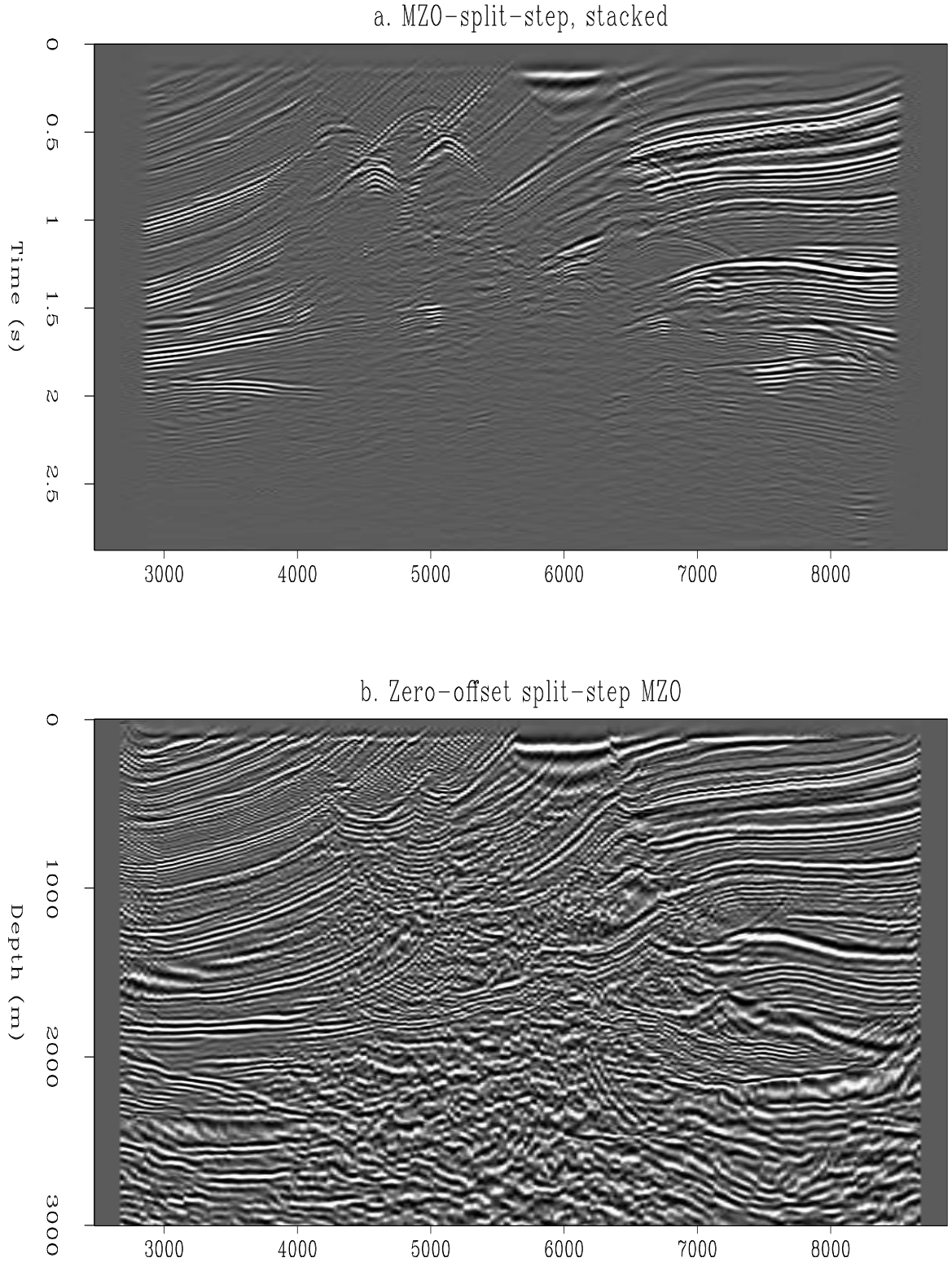

Figure 1.16: Stacked data after MZO-split-step, and the migrated image.
a. MZO-split-step stacked data.
b. Zero-offset split-step migration applied to the stacked data. chapter3-marmMZOFFTsplit [CR]

1.3.3 Application to seismic data

If MZO offers some improvements to media with lateral velocity variations, it is a second-order correction to depth-only velocity variation media like the Gulf of Mexico. Figure ?? compares the stacked sections of a Gulf of Mexico dataset. The common-midpoint spacing is 25 m, and the maximum offset is 3200 m.

Figures ?? and ?? display the zero-offset migrated data. The areas were MZO is expected to perform better than the standard sequence of NMO followed by DMO are the zones with fast velocity variations, near the salt boundaries. The right flank of the salt dome is imaged better after MZO, and so is the are the sediments on the right side of the salt dome. There is better reflector continuity and a better definition of the reflectors resulting in a crisper, better focused image after MZO. These improvements can be seen better in Figure ??, which is just a magnification of the upper right part of Figure ??.

Overall, I conclude that since MZO is a second order improvement in depth variable velocity, in most area of the Gulf of Mexico, the industry standard processing sequence of stacking after NMO and DMO will provide an adequate image. MZO offers modest improvements to data in mild depth velocity variations media, though I expect better results in strong depth velocity variations or lateral velocity variations. Hawkins (1994) also confirms the fact that NMO and DMO is an appropriate processing sequence even in the North Sea Central Graben area, were conventional processing performed better than expected. For laterally varying media the velocity dependent MZO becomes a first order correction, but further work is needed to define an operator that produces identical results to prestack migration.

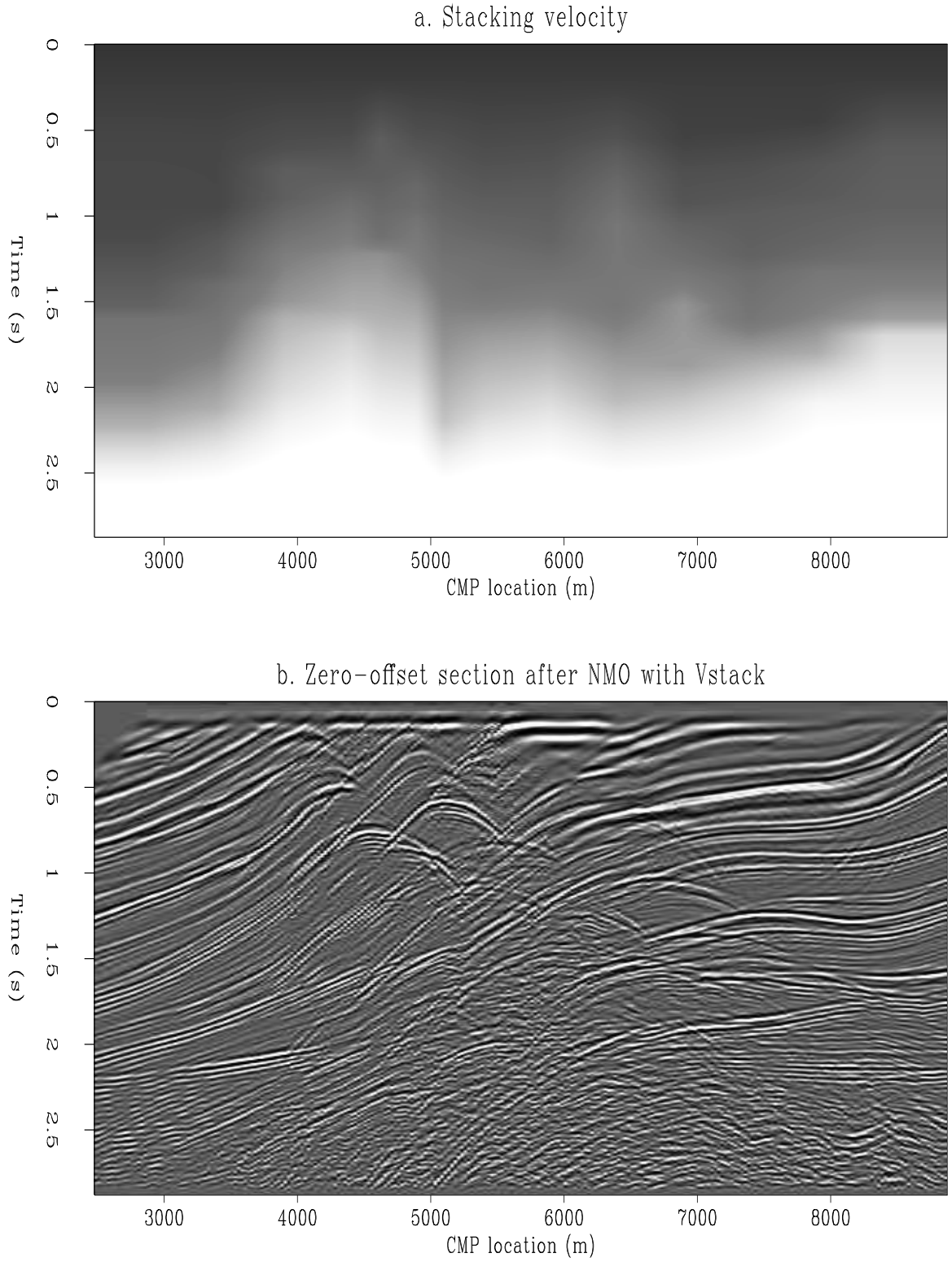

Figure 1.17: The stacking velocity and the stacked data after NMO.
a. Stacking velocity.
b. NMO with best stacking velocity and stacking. chapter3-VstackandNMOst [ER]

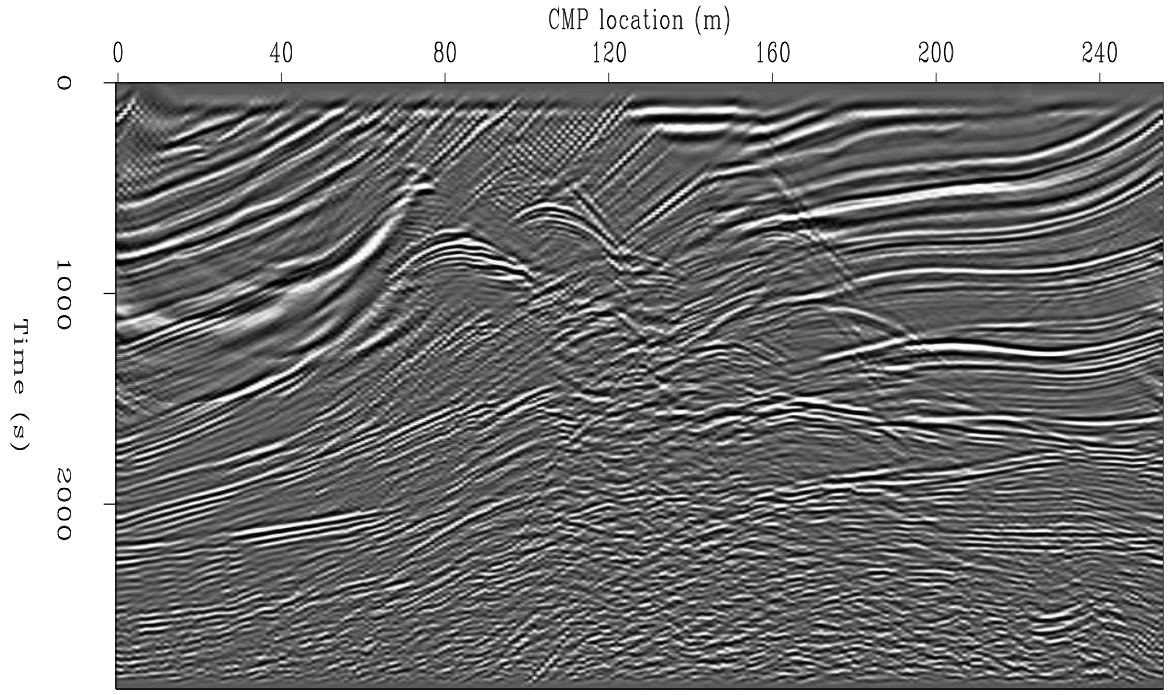

a. Zero-offset section after NMO and DMO

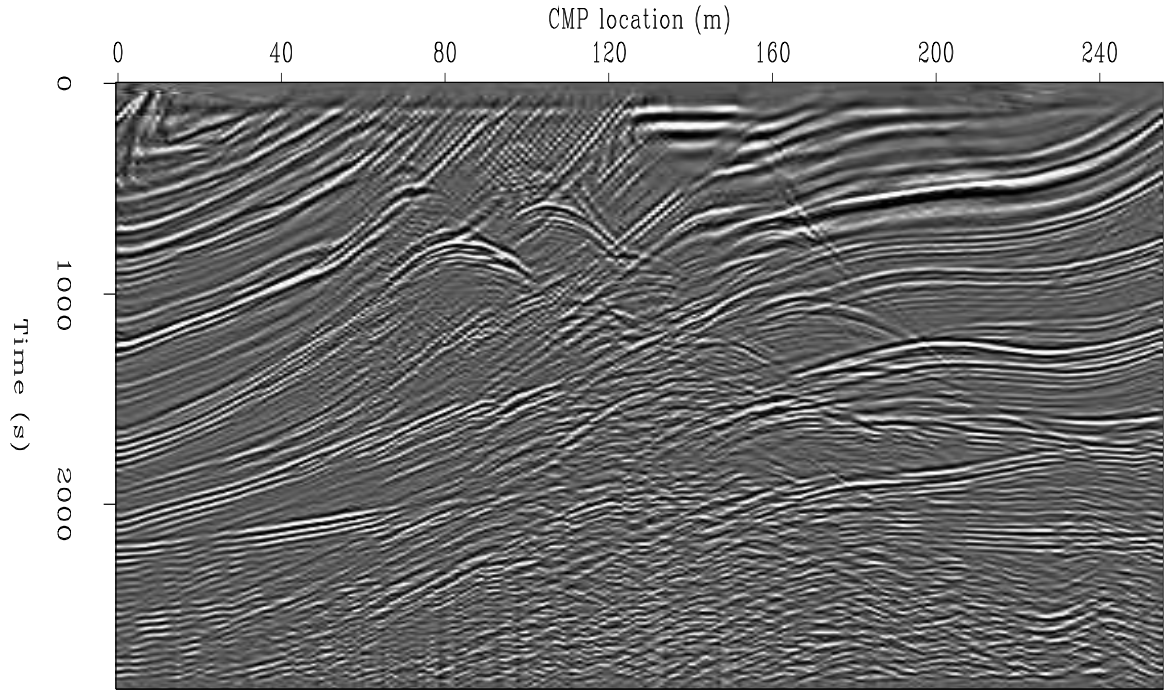

b. Zero-offset section after MZO

Figure 1.18: Stacked data after DMO and MZO.
a. NMO with best stacking velocity, DMO and stacking.
b. NMO with best stacking velocity, INMO with average $v(t)$, MZO with $v(t)$ and stacking. chapter3-DMOandMZOst [CR]

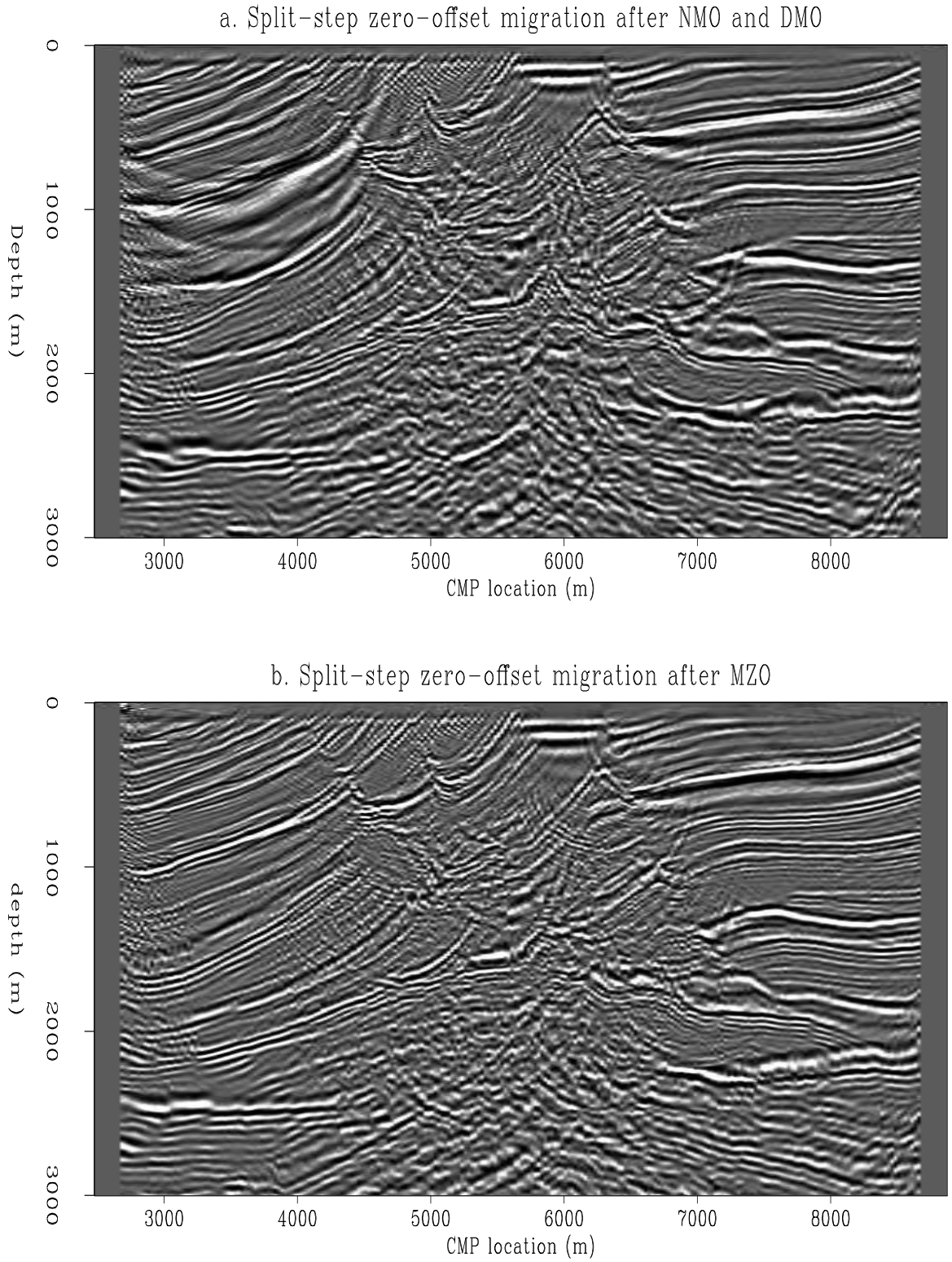

Figure 1.19: Zero-offset migration of the Marmousi data using the stacking velocity for NMO.
a. NMO with best stacking velocity, DMO, stacking, and split-step zero-offset migration.
b. NMO with best stacking velocity, INMO, MZO, stacking, and split-step zero-offset migration. chapter3-DMOandMZOmig [CR]

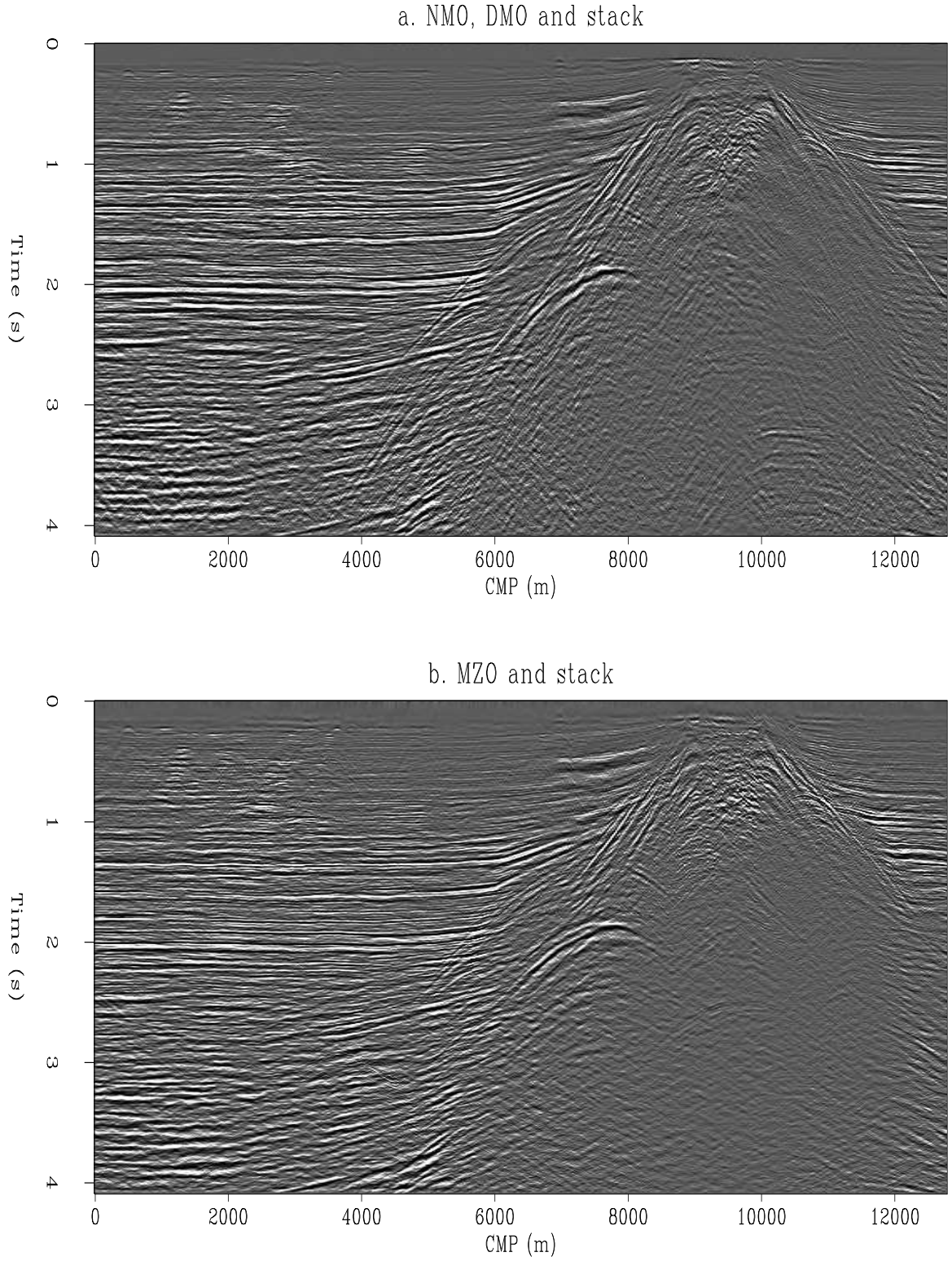

Figure 1.20: Comparison between DMO and MZO stacked data.
Gulf of Mexico data after NMO, DMO, and stacking.
Gulf of Mexico data after NMO with the laterally varying stacking velocity, inverse NMO with a laterally invariant velocity, MZO using the same laterally invariant velocity, and stacking. chapter3-GulfMZOst [CR]

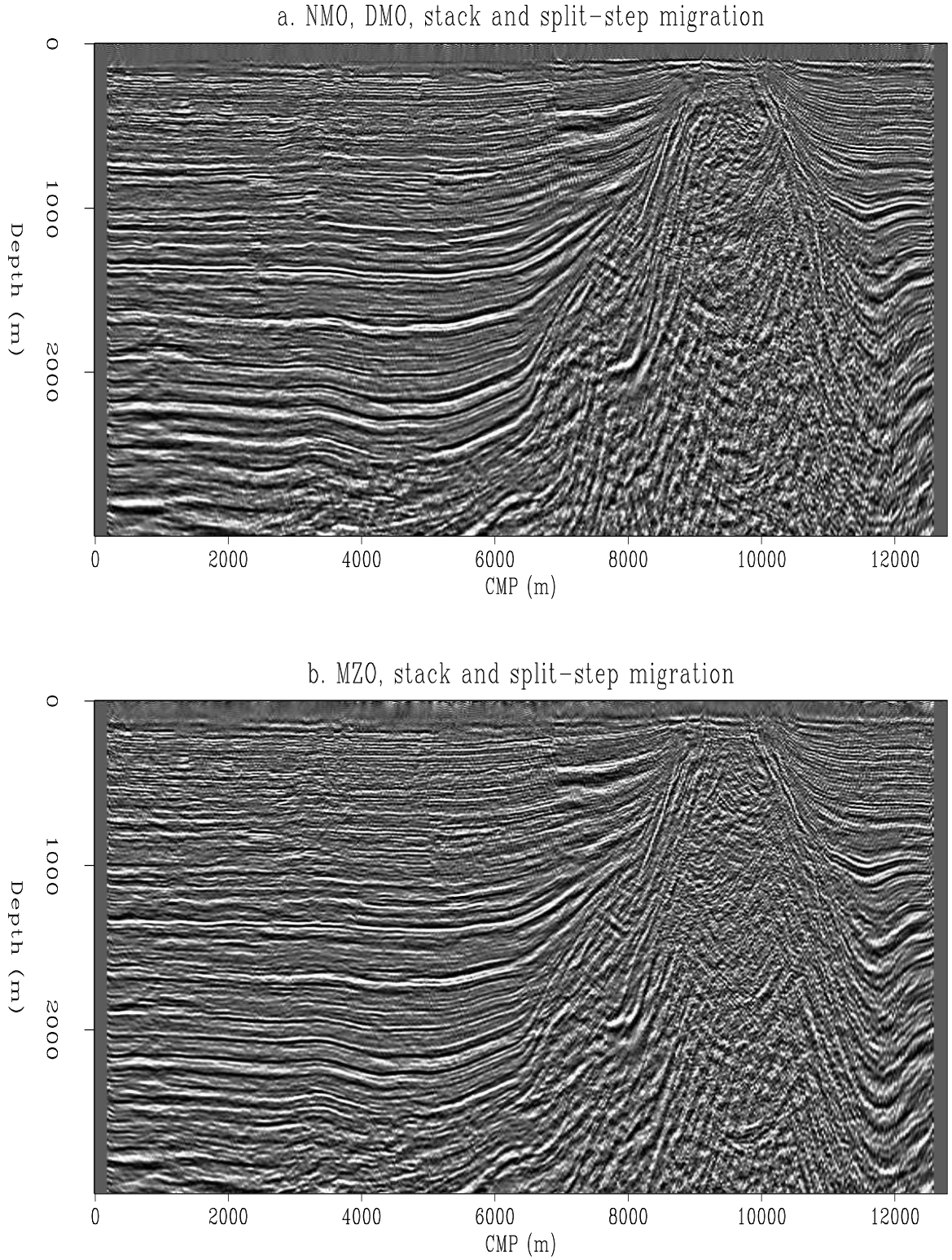

Figure 1.21: Comparison between DMO and MZO stacked and migrated data.
a. Gulf of Mexico data after NMO, DMO, stacking and split-step migration.
b. Gulf of Mexico data after NMO with the laterally varying stacking velocity, inverse NMO with a laterally invariant velocity, MZO using the same laterally invariant velocity, stacking and split-step migration. chapter3-GulfMZOmig [CR]

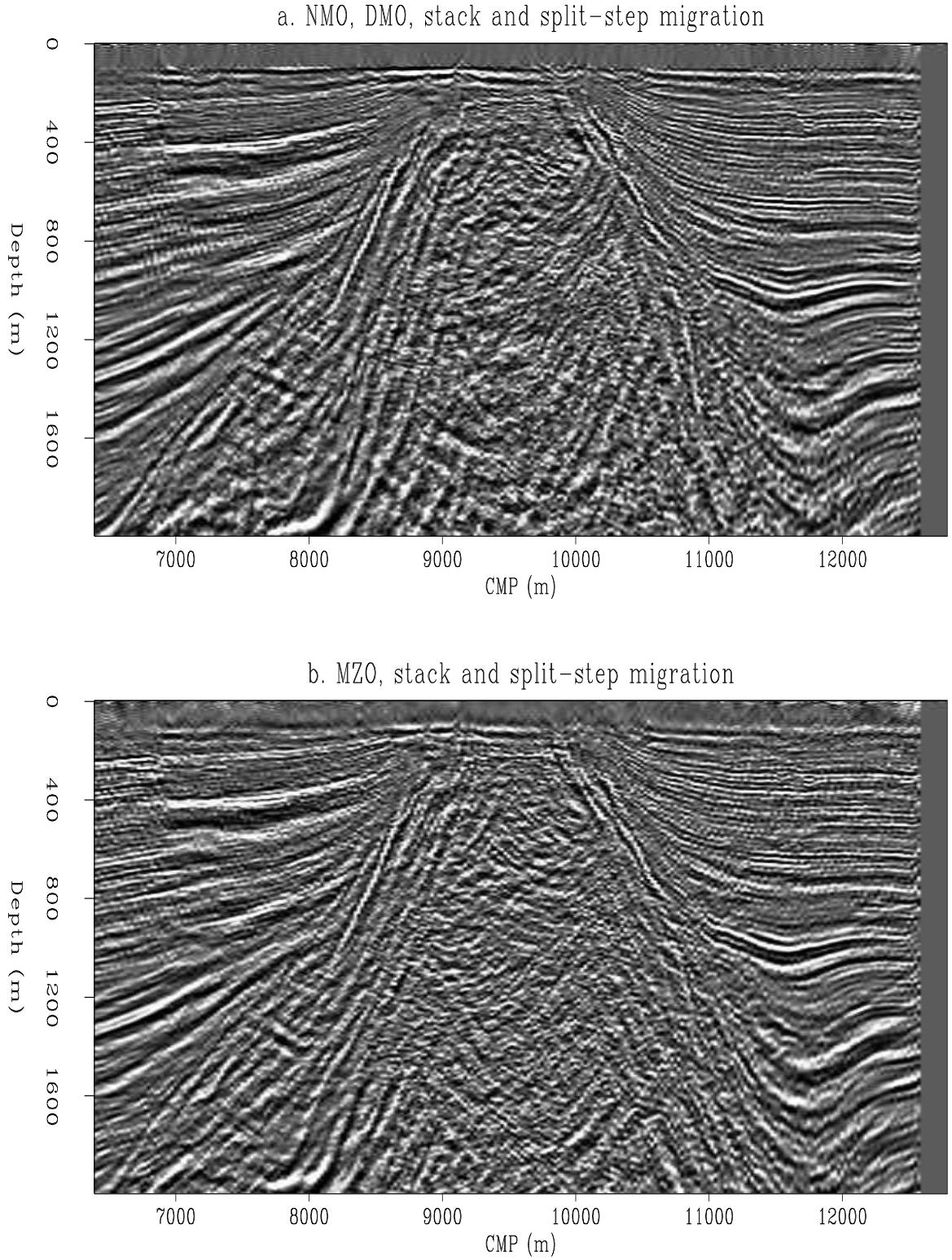

Figure 1.22: Comparison between DMO and MZO stacked and migrated data, detail area.
a. Data after NMO, DMO, stacking and split-step migration.
b. Data after NMO with the laterally varying stacking velocity, inverse NMO with a laterally invariant velocity, MZO using the same laterally invariant velocity, stacking and split-step migration. chapter3-GulfMZOmigcut [CR]